

Extracting weak magnetic contrast from complex background contrast in plan-view FeGe thin films

Binbin Wang^{a,b}, Núria Bagués^b, Tao Liu^c, Roland K. Kawakami^c, David W. McComb^{a,b,*}

^a Department of Materials Science and Engineering, The Ohio State University, OH 43210, United States

^b Center for Electron Microscopy and Analysis, The Ohio State University, OH 43212, United States

^c Department of Physics, The Ohio State University, OH 43212, United States

ARTICLE INFO

Keywords:

Lorentz TEM
Lorentz STEM
4D-STEM
Skyrmion
FeGe
Magnetic contrast

ABSTRACT

The desire to design and build skyrmion-based devices has led to the need to characterize magnetic textures in thin films of functional materials. This can usually be achieved through the Lorentz transmission electron microscopy (LTEM) and the Lorentz scanning transmission electron microscopy (LSTEM) in thin film cross-section and single crystal specimens. However, direct imaging of the magnetic texture in plan-view samples of thin (< 50 nm) films has proved to be challenging due to the complex “background” contrast associated with the microstructure and defects, as well as contributions from bending of the specimens. Using a mechanically polished 35 nm plan-view FeGe thin film, we have explored three methods to extract magnetic contrast from the complex background contrast observed; (1) background subtraction in defocused LTEM images, (2) frequency filtered CoM-DPC reconstructed from LSTEM datasets and 3) registration of 4D-STEM datasets acquired at different tilt angles. Using these methods, we have successfully implemented real space imaging of both the helical phase and skyrmion phase. The ability to understand nanoscale magnetic behavior from plan-view thin films is a fundamental step towards development of highly integrated spin electronics.

1. Introduction

Real space imaging of magnetic textures such as skyrmions is important for characterization and development of magnetic and spintronic devices. Magnetic skyrmions are topologically protected particle-like spin textures ranging in size from nanometers to micrometers [1,2]. To visualize such magnetic textures, the transmission electron microscopy (TEM) is an indispensable tool. In the TEM, phase contrast associated with a magnetic field in the sample, is caused by the magnetic vector potential inside and around the sample. The 2-D gradient of the integrated magnetic induction along the beam direction can then be obtained from the magnetic contrast maps, which will be referred as integrated magnetic induction (IMI) maps hereinafter. A general term for imaging magnetic textures in electron microscopy is called Lorentz mode. Over the last half-century, a number of techniques have been explored to characterize magnetic phase contrast in Lorentz mode, including Fresnel imaging, Foucault imaging, electron holography, center of mass differential phase contrast (CoM-DPC) andptychography [3–9]. All these techniques have been successfully used to observe topological magnetic configurations in a variety material systems, such as

vortices, bubbles and skyrmions [10,11]. However, in thin films and multilayers, it can be challenging to differentiate weak magnetic contrast from that associated with complex microstructure, e.g. grain boundary, thickness variation. Consequently, methods to enhance and extract the weak magnetic contrast in such thin film samples are necessary. Generally, this can be realized in the post-processing of image datasets. For example, in Lorentz TEM (LTEM) images, the background subtraction method and Fourier filter have been demonstrated to be effective in single crystals, and in some cases, thin films [12,13]. For Lorentz scanning TEM (LSTEM) data, methods, such as frequency filtering by selecting different scattering angle ranges in the transmitted disk [14–16] and specimen-tilt series averaging DPC STEM [17] have been explored.

Here we explore the use of LTEM and LSTEM for imaging spin textures in epitaxial FeGe thin films grown on Si (111) for skyrmion based spintronic applications. FeGe is a chiral magnet with the B20 structure and a Curie temperature (T_c) of ~ 223 K. The epitaxial films are polycrystalline with (111) out-of-plane orientation and grains with $\pm 30^\circ$ rotations in plane. In single crystal FeGe and in cross-sections of epitaxial thin films, transitions between helical and skyrmion phases

* Corresponding author at: Department of Materials Science and Engineering, The Ohio State University, OH 43210, United States.

E-mail addresses: wang.10255@osu.edu (B. Wang), mccomb.29@osu.edu (D.W. McComb).

have been observed by tuning magnetic field and temperature [18,19]. Theoretical simulations indicate that skyrmion or chiral bobber phases will be observed in the plan view FeGe thin film under a magnetic field that is in the direction of film growth [19]. However, a recent report claimed that magnetic textures could not be observed experimentally in the plan-view FeGe thin film on a Si substrate due to substrate-induced tensile strain [15]. To check the disagreement between the experimental results and theoretical modeling, it is important to carefully extract weak magnetic phase contrast from the complex background. In this contribution, we have explored three methods to extract the magnetic texture from a plan view sample of an MBE grown polycrystalline FeGe thin film prepared using wedge-mechanical polishing. These methods including (1) background subtraction in defocused LTEM images, (2) frequency filtered CoM-DPC reconstructed from LSTEM datasets and (3) registration of 4DSTEM datasets acquired at different tilt angles. Through these phase enhancement processes we have demonstrated the possibility of extracting weak magnetic contrast from complex background contrast in plan-view thin films. Using real space images, we have successfully revealed the presence of both helical and skyrmion phase in FeGe thin films on Si (111) substrate. In the following sections, we will compare and summarize advantages/disadvantages of each approach to this challenging problem.

2. Material and methods

2.1. Sample preparation and structural characterization

The 35 nm FeGe sample used in this study was grown on a Si (111) substrate in an MBE chamber with base pressure of 2×10^{-10} Torr. To remove the top native oxide layer, the Si (111) substrate was immediately loaded into the chamber after a two min etching process in buffered HF, and then annealed in vacuum at 800 °C for 20 min. A two-step growth method was used to improve the quality of FeGe film. Initially, a 3 nm FeGe buffer layer was grown at 340 °C and then annealed at 370 °C for 30 min, then a 32 nm thick film was grown at 340 °C.

To perform the structural characterization of the sample, a cross-section specimen was prepared by Ga ion milling in a FEI Helios NanoLab 600 DualBeam focused ion beam (FIB) operated at 30 kV and then 5 kV. Final polishing was performed using a Fischione NanoMill using 900 V and then 500 V Ar ions to remove any amorphous surface damage created in the FIB. Annular dark field (ADF) STEM imaging was performed using a Thermo Scientific Themis Z S/TEM at 300 kV. An ADF-STEM image from a cross-section specimen of FeGe thin film is presented in Fig. 1a. The FeGe thin film adopts a B20 structure and grows epitaxial on the Si substrate, following a $[111]_{\text{Si}}/[111]_{\text{FeGe}}$ out-of-plane direction and $[11\bar{2}]_{\text{Si}}/[1\bar{1}0]_{\text{FeGe}}$ in-plane direction.

Plan-view specimens were prepared by wedge-mechanical polishing.

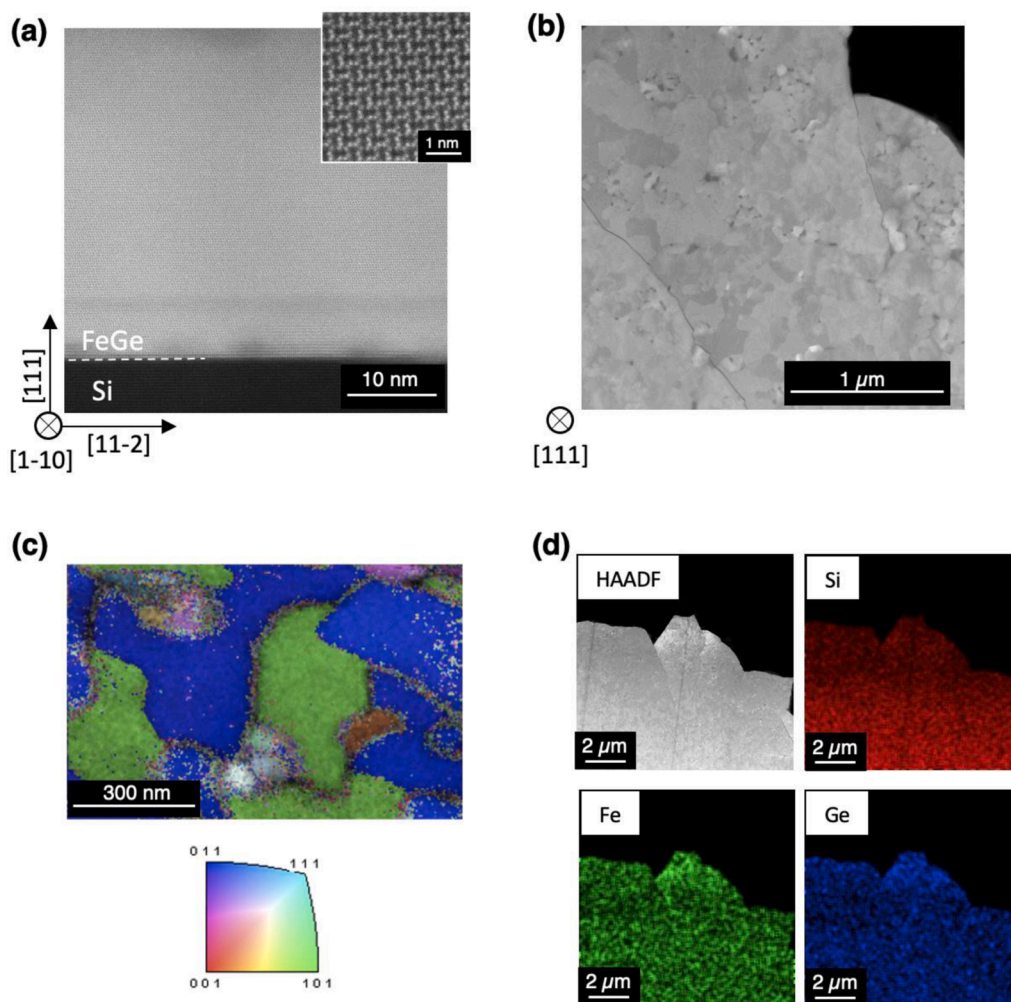


Fig. 1. Structural characterization of Si//FeGe (35 nm) thin film. (a) Cross-sectional ADF STEM image along $[11\bar{2}]_{\text{Si}}/[1\bar{1}0]_{\text{FeGe}}$ direction. Insert: a high magnification image from the FeGe thin film showing B20 structure. (b) Plan-view ADF STEM image, (c) in-plane TKD map showing in-plane alignment of the grains and (d) elemental XEDS maps.

ADF-STEM imaging and x-ray energy dispersion spectroscopy (XEDS) analysis were performed using image-corrected FEI Titan3™ G2 60–300 S/TEM at 300 kV. ADF-STEM images from the plan-view specimens demonstrate the specimens are electron transparent and the epitaxial films have large grains with $\pm 30^\circ$ rotations in plane as observed by transmission kikuchi diffraction (TKD) patterns (Fig. 1c) performed using ThermoFisher Apreo LoVac Field Emission Scanning Electron Microscope equipped with an EDAX Hikari Pro-EBSD camera using the OIMDC software. XEDS analysis show the Si substrate was not completely removed (Fig. 1d).

2.2. Lorentz EM experiments and magnetic contrast enhancement methods

The Fresnel mode LTEM and LSTEM experiments were conducted using an image-corrected FEI Titan3™ G2 60–300 S/TEM at 300 kV. In Lorentz mode, the magnetic field applied to the sample is tuned by changing the current of the objective lens. In order to observe skyrmions or the helical phase, the temperature (T) and magnetic field (B) were chosen from the B vs T phase diagram for FeGe single crystals reported in previous works [20]. The specimen temperature during the experiment was controlled using a liquid nitrogen cryo-holder (Gatan 636) while the magnetic field was varied by gradually changing the objective lens current of the microscope. In all the experiments, the sample was zero field cooled (± 10 mT remanent field). The experimental workflows for different magnetic contrast enhancement methods are summarized in the sub-sections below.

$$CTF\left(\frac{Q_p}{\alpha}\right) = \begin{cases} \frac{4}{\pi} \left[\cos^{-1}\left(\frac{Q_p}{2\alpha}\right) - \cos^{-1}\left(\frac{Q_p}{\alpha}\right) + \frac{Q_p}{\alpha} * \sqrt{1 - \frac{Q_p^2}{\alpha^2}} - \frac{Q_p}{2\alpha} * \sqrt{1 - \left(\frac{Q_p}{2\alpha}\right)^2} \right], & 0 \leq Q_p \leq \alpha, \\ \frac{4}{\pi} \left[\cos^{-1}\left(\frac{Q_p}{2\alpha}\right) - \frac{Q_p}{2\alpha} * \sqrt{1 - \left(\frac{Q_p}{2\alpha}\right)^2} \right], & \alpha < Q_p \leq 2\alpha \end{cases}$$

2.2.1. Background subtraction in defocused LTEM images

The majority of non-magnetic “background contrast” in the images arises from crystalline defects (grain boundaries), sample bending artifacts (bend contours), and residual particles from mechanical polishing. Note that background contrast caused by defects and residual particles can contribute intensity components related to both absorption and phase, so they depend on defocus. To reduce as much as possible the background contrast, over/under focused LTEM images are acquired from the same sample region under different conditions of T and B to emphasize magnetic contrast (target images) or only background contrast (background images). Due to the image corrector, our microscope has a lower spherical aberration coefficient (C_s) than normal system, and therefore higher resolution achievable in the image corrected TEM. The image corrector is also used to correct distortion in images. To optimize the correction, we minimized astigmatism and misalignment in the diffractograms obtained from defocused LTEM images using the fast Fourier Transformation. This was conducted with our plan-view sample of polycrystalline FeGe thin film. The intensity scale for each image is normalized to be 0–1 to balance the electron dose change in images. The target images are aligned with a selected background image using Etomo [21], where the features in these images are non-linearly aligned using automatic and manual alignments. Note that due to changes in the pixel size in the aligned image, the scale bar needs to be adjusted according to the reference features. Finally, to get the best match, different background images acquired at varied optical parameters were tested. Hot spots due to pixel level mismatch are removed

using a Gaussian blur function ($\sigma = 1 - 2$) as necessary.

In Section 3.1, the non-background subtraction LTEM focal series images were used to reconstruct the magnetization maps using the QPt software package which utilizes the transport-of-intensity equation (TIE) [22]. Since QPt algorithm includes a division of the Fourier transform of image intensity by a squared modulus of frequency, the noise at low frequency is amplified and results in a spurious background phase shift variation that is not physical. To reveal fine details of the phase in relatively high spatial frequencies, we applied a high-pass filter in the IMI images.

2.2.2. Frequency filtered CoM-DPC reconstructed from LSTEM 4D-STEM datasets

4D-STEM refers to recording convergent beam electron diffraction (CBED) patterns at each probe position in a real space image [8]. The technique has been widely explored in structural and electronic investigations [8,23,24] as well as for the characterization of electric/magnetic fields [25–27]. In LSTEM mode, the in-plane magnetic field of the specimen can be measured from the momentum transfer in CBED patterns according to the theory of Ehrenfest [28]. In this work, the momentum transfer in CBED patterns is measured using CoM-DPC, where the relative shift of center of mass of the CBED pattern can be related to momentum transfer and thus to the magnetic field [29].

The contrast transfer function (CTF) of DPC determines how much phase signal at different spatial frequencies is transmitted to the image and depends on both convergence semi-angle (α) and collection semi-angle (β) [26,30,31]. Assuming **no loss of coherence**, the maximum CTF of DPC using pixelated detector can be given by [30]:

where the Q_p is spatial frequency. For CoM-DPC reconstructed from regions with different collection angles, as shown in Fig. 2a and 2b, there are high and low critical frequencies. Since the signal contrast in CoM-DPC comes from the phase difference in the overlapping area of the disk, only the spatial frequency between the high and low critical frequencies will be transferred to the virtual detector area. Fig. 2c shows the cumulative contribution of successive annular rings to the CTF of full transmitted disk DPC. The central region of the transmitted disk ($\beta \approx 0$) is transferring spatial frequencies around α , while the transmitted disk edge region ($\beta \approx \alpha$) includes the spatial frequency range from 0 to 2α . By optimizing convergence angles and collection angles for reconstruction, it is possible to select target frequencies in CoM-DPC. To extract weak magnetic contrast from background contrast, we want to select spatial frequencies associated with magnetic textures while excluding spatial frequencies contributing to background contrast.

This simplified description of the CTF of DPC does not consider the influence of coherence, the potential function, or the probe size. For example, Cao et al. proved that the CTF of DPC can origin from disk shift and/or intensity distribution within the disk, depends on sample potential models [16]. If the sample has a linear ramp (probe size \ll function size) then disk drift dominates, while if the sample potential is a delta function (probe size \gg function size) the intensity distribution within the disk will change. In the first case, the magnetic contrast can be enhanced by tracking only the edge of the bright field disk, serving as a low-pass filter [14]. In the latter case, the spatial frequency selection depends on the collection angle as shown in Fig. 2. We note that Nguyen

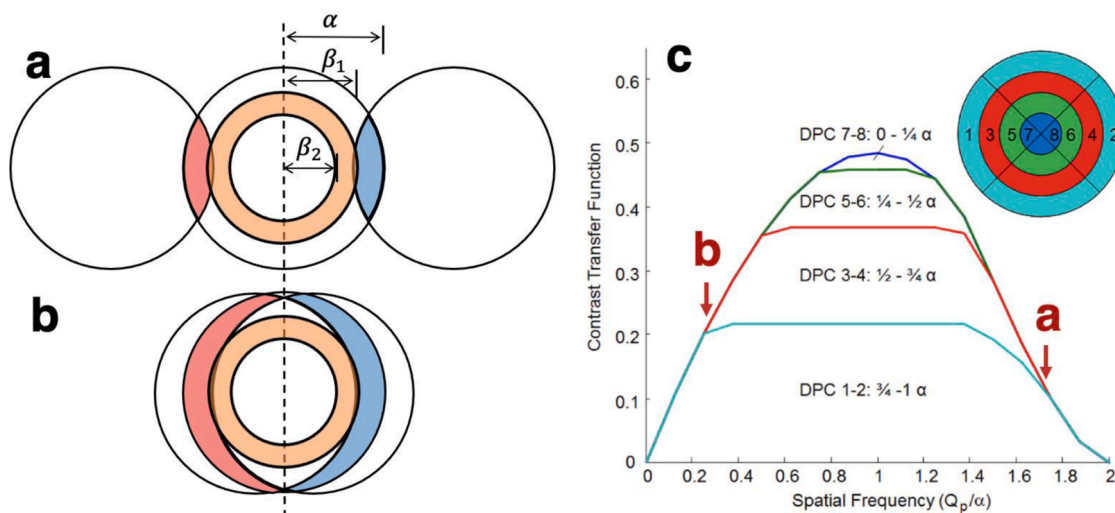


Fig. 2. The illustration of high critical frequency (a) and low critical frequency (b) in the reconstruction of CoM-DPC using a virtual annular detector. Disk-overlap regions with anti-phase are indicated in red and blue colors. β_1 and β_2 are inner and outer collection angles of virtual detector. (c) is the cumulative contribution of successive annular rings to the CTF of full quadrant DPC, which is adapted from reference [30]. The inner and outer collection angles of each annular segment are $0 - \frac{1}{4}\alpha$, $\frac{1}{4} - \frac{1}{2}\alpha$, $\frac{1}{2} - \frac{3}{4}\alpha$, $\frac{3}{4} - \alpha$. The 4 areas separated by the plots represent the fractional CTF of the four rings and summing up the four areas leads to the full quadrant DPC. The red arrows in c indicate the cases of high (a) and low (b) critical frequency when the inner and outer collection angles of the annular segment is $\frac{1}{2} - \frac{3}{4}\alpha$ (For interpretation of the references to color in this figure, the reader is referred to the web version of this article.).

et al. tried to separate the magnetic signals from short-range potentials based on the assumption that magnetic field is long-range signal relative to the probe size (a few nanometers), while changes in grain contrast are short range [15]. In this work, we found using the CTF in Fig. 2 for frequency selection enabled better separation of the magnetic signal from the background signal. This may be reasonable considering the electron beam deflection (β_s) is proportional to $B_0 t$ in the linear ramp model, where B_0 is the local magnetic field and t is sample thickness. To obtain a signal sufficiently higher than Poisson noise, there is a minimum deflection angle $\beta_L = \pi\alpha/4\sqrt{n}$ which is determined by the convergence angle α and the dose n [15]. When the magnetic signal is weak ($\beta_s < \beta_L$), the disk shift cannot be resolved even if the probe size is smaller than the feature size. In addition, when the sample potential has a gradient (i.e. the field within the sample is not constant), there is no visible disk displacement in the simulation, but a COM displacement is observed due to intensity redistribution [29,32].

A summary of spatial frequency ranges with different α and β is presented in Table 1, calculated from Bragg's law with a relativistic corrected wavevector at different acceleration voltages [33]. In this

work, convergence semi-angles of 60 and 390 μrad are used at 300 kV. CoM-DPC images and associated virtual bright field (BF) images are reconstructed from 4D-STEM datasets using a program based on py4D-STEM and pixSTEM [34,35].

2.2.3. Registration of 4D-STEM datasets acquired at different tilt angles

Registration of DPC STEM images acquired at different tilt angles has been explored previously as a path to suppress diffraction contrast in DPC images [17]. This is because the diffraction contrast in these images is sensitive to crystal orientation and thus random diffraction contrast will vanish by averaging specimen-tilt image series. Here we extended this method to Lorentz 4D-STEM datasets following the workflow described in references [36,37]. The workflow is illustrated in Fig. 3. Firstly, the CBED patterns in 4D-STEM datasets are aligned to remove any shift of the transmitted disk. BF images are reconstructed from each dataset and registered using SmartAlign [38]. In the prior report it was assumed that the diffraction contrast in the DPC image varies randomly with the tilt angle of the sample. Therefore, for the final image registration, each image in the image series should be treated equally. However, this assumption does not hold true in many cases. For

Table 1

The selected real spatial frequency ranges in reconstructed CoM DPC images using different convergence semi-angles α and collection semi-angle ranges β . The real spatial frequency ranges are given in a format of (high critical frequency, low critical frequency), where only spatial frequencies between these two critical numbers are transferred into DPC images.

$\beta \alpha$	Spatial frequencies (nm)							
	100 kV				300 kV			
	$(0 - \frac{1}{4})\alpha$	$(\frac{1}{4} - \frac{1}{2})\alpha$	$(\frac{1}{2} - \frac{3}{4})\alpha$	$(\frac{3}{4} - 1)\alpha$	$(0 - \frac{1}{4})\alpha$	$(\frac{1}{4} - \frac{1}{2})\alpha$	$(\frac{1}{2} - \frac{3}{4})\alpha$	$(\frac{3}{4} - 1)\alpha$
25 μrad	(118.4, 394.8)	(98.7, 592.2)	(84.6, 1184.4)	(74.0, ∞)	(63.0, 210.0)	(52.5, 315.0)	(45.0, 630.0)	(39.4, ∞)
50 μrad	(59.2, 197.4)	(49.4, 296.1)	(42.3, 592.2)	(37.0, ∞)	(31.5, 105.0)	(26.3, 157.5)	(22.5, 315.0)	(19.7, ∞)
60 μrad	(49.4, 164.5)	(41.1, 246.8)	(35.3, 493.5)	(30.8, ∞)	(26.3, 87.5)	(21.9, 131.2)	(18.8, 262.3)	(16.4, ∞)
100 μrad	(29.6, 98.7)	(24.7, 148.1)	(21.2, 296.1)	(18.5, ∞)	(15.7, 52.5)	(13.1, 78.7)	(11.3, 157.5)	(9.8, ∞)
300 μrad	(9.9, 32.9)	(8.2, 49.3)	(7.1, 98.7)	(6.2, ∞)	(5.3, 17.5)	(4.3, 26.3)	(3.8, 52.5)	(3.3, ∞)
390 μrad	(7.6, 25.3)	(6.3, 38.0)	(5.4, 75.9)	(4.8, ∞)	(4.0, 13.5)	(3.4, 20.2)	(2.9, 40.4)	(2.5, ∞)
500 μrad	(5.9, 19.7)	(4.9, 29.6)	(4.2, 59.2)	(3.7, ∞)	(3.2, 10.5)	(2.6, 15.7)	(2.3, 31.5)	(2.0, ∞)
1 mrad	(3.0, 9.9)	(2.5, 14.8)	(2.1, 29.6)	(1.9, ∞)	(1.6, 5.3)	(1.3, 7.9)	(1.1, 15.7)	(1.0, ∞)
5 mrad	(0.6, 2.0)	(0.5, 3.0)	(0.4, 5.9)	(0.4, ∞)	(0.3, 1.0)	(0.3, 1.6)	(0.2, 3.2)	(0.2, ∞)
10 mrad	(0.3, 1.0)	(0.3, 1.5)	(0.2, 3.0)	(0.2, ∞)	(0.2, 0.5)	(0.1, 0.8)	(0.1, 1.6)	(0.1, ∞)

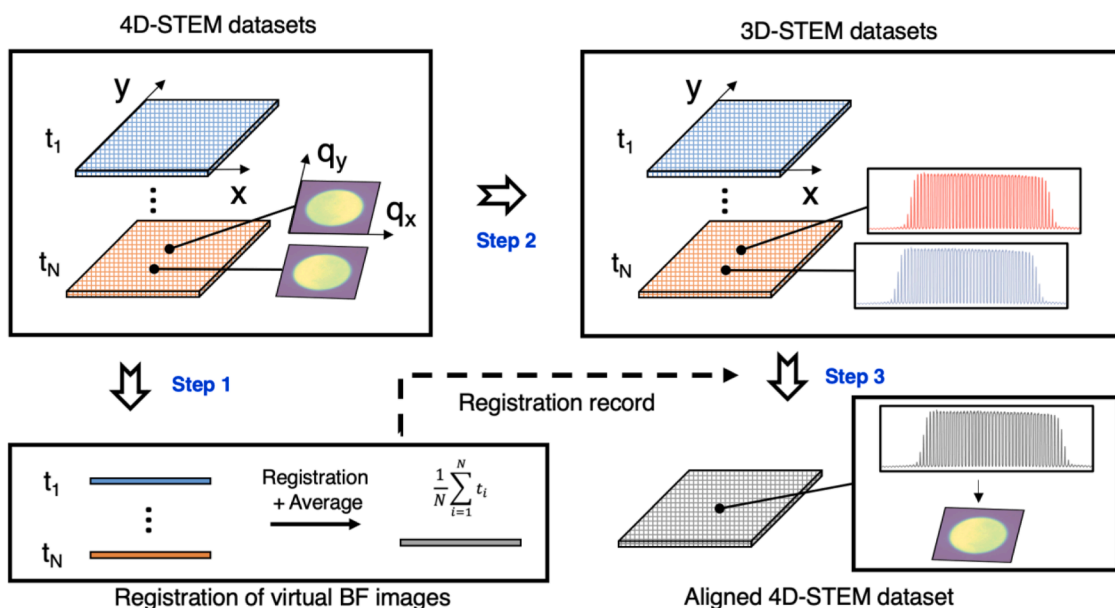


Fig. 3. Flowchart of registration of 4D-STEM datasets. In step 1, virtual BF images are reconstructed from 4D-STEM datasets (t_1, \dots, t_N) and then aligned using non-rigid registration. In this process, the registration history of virtual BF images is recorded. In step 2, the original 4D-STEM datasets are transformed into 3D-STEM datasets (GMS3 type). After that, in step 3, these 3D-STEM datasets are aligned and averaged using the registration record in step 1 and transformed back to one 4D-STEM dataset.

example, the contrast caused by sample bending during sample preparation and diffraction contrast from grain boundaries are not randomly distributed. Thus, in some cases diffraction contrast sometimes cannot be suppressed as it may overlap in adjacent images in the series. Compared with DPC acquired from segmented detectors, 4DSTEM datasets requires more storage and processing time. To minimize diffraction contrast in this work, the datasets used for registration were selected from 4DSTEM datasets series obtained with different sample tilt angles (in a range of $\pm 2^\circ$) with a step of 0.5° . The selection is based on the distribution of bend contrast and grain contrast in reconstructed virtual BF images.

3. Results

3.1. Background subtraction in defocused LTEM image

Three main sources of non-magnetic background contrast (grains, bend contours, and residual particles from mechanical polishing) can be readily seen in the in-focus LTEM images in Fig. 4a,b. First, we confirm the presence of magnetic textures in the material by adjusting the microscope to over-focus LTEM conditions (Fig. 4c,d). The magnetic phase diagram predicts we should observe the helical phase at $B = 0$ mT (Fig. 4c) and the skyrmion lattice at $B \approx 80$ mT (Fig. 4d) at 240 K. The presence of magnetic textures in defocused images can be seen, though the details are still obscured by background contrast. The in-focus and over-focus images were combined with under-focus images (not shown) to reconstruct the IMI maps using QPt [22], as presented in Fig. 4e and f. The image sequence is aligned by affine alignment, and a high-pass filter is applied to phase contrast to filter out low spatial frequencies. This reconstruction confirms the transition from helical to skyrmion phase in certain areas of the image, e.g. inside the white boxes. However, background contrast contributions clearly impact the reconstruction, making it difficult to see the magnetic phases clearly or quantify the magnetic fields accurately.

To isolate the magnetic texture from the background contrast, we apply the image subtraction method described in Section 2.2.1. Based on the magnetic phase diagram for FeGe single crystal thin films [17], no magnetic textures are expected in FeGe above $T_c \approx 280$ K, meaning

images collected at room temperature (RT) and $B = 0$ mT can be used to isolate background contrast features (Fig. 5a). These images can be compared with those collected at $T \approx 240$ K with $B = 0$ mT (Fig. 5b) and $B = 130$ mT (Fig. 5c), and subtracted to isolate the magnetic features. After applying this method, the helical phase at 0 mT is readily apparent, and we can distinguish between skyrmions with different chirality based on their bright/dark contrast, as seen in Fig. 5d and 5e. Note, these images were acquired at same defocus as both magnetic and non-magnetic background contrast can be defocus sensitive. While this image subtraction method is effective for separating magnetic contrast from most of the background contrast features, especially grain boundaries and residual particles, it is not perfect; contrast from bend contours is still visible, and it is sometimes enhanced because of changes in diffraction condition at different temperatures. Slight variations in optical conditions, such as defocus, will also introduce additional contrast such as Fresnel fringes.

To explore further the effectiveness of this method, we acquired additional images at different T and B conditions. At $T = 240$ K, we expect the skyrmion phase to be present at $B \approx \pm 100$ mT, and the sample magnetization to be saturated at $B \approx \pm 300$ mT. Fig. 6a shows the area of interest at $T = 240$ K and $B = -100$ mT. Fig. 6b–e show the resulting defocused LTEM images after subtracting background contrast images acquired at (b) RT and 0 mT, (c) RT and -100 mT, (d) 240 K and 300 mT, and (e) 240 K and -300 mT, respectively.

In all cases, contrast from the magnetic textures is enhanced while contrast from residual particles is reduced. Consistent with previous experiments, bend contours introduce substantial artifacts when subtracting images collected at different temperatures. This suggests the optimal approach is to use background images acquired at constant T but different B. We note that even at constant T, there are important differences in the final images depending on the relative sign of the applied field at saturation (Fig. 6d and e). Subtracting opposite sign images results in readily apparent skyrmions, bend contours, and an additional contrast (yellow arrows in Fig. 6d); which is also weakly observed in images obtained after subtraction background images at RT and $B = 0$ (Fig. 6b and c). However, this additional contrast is not seen in final images where the saturation field has the same sign (Fig. 6e). One explanation for the origin of this additional contrast is the grains present

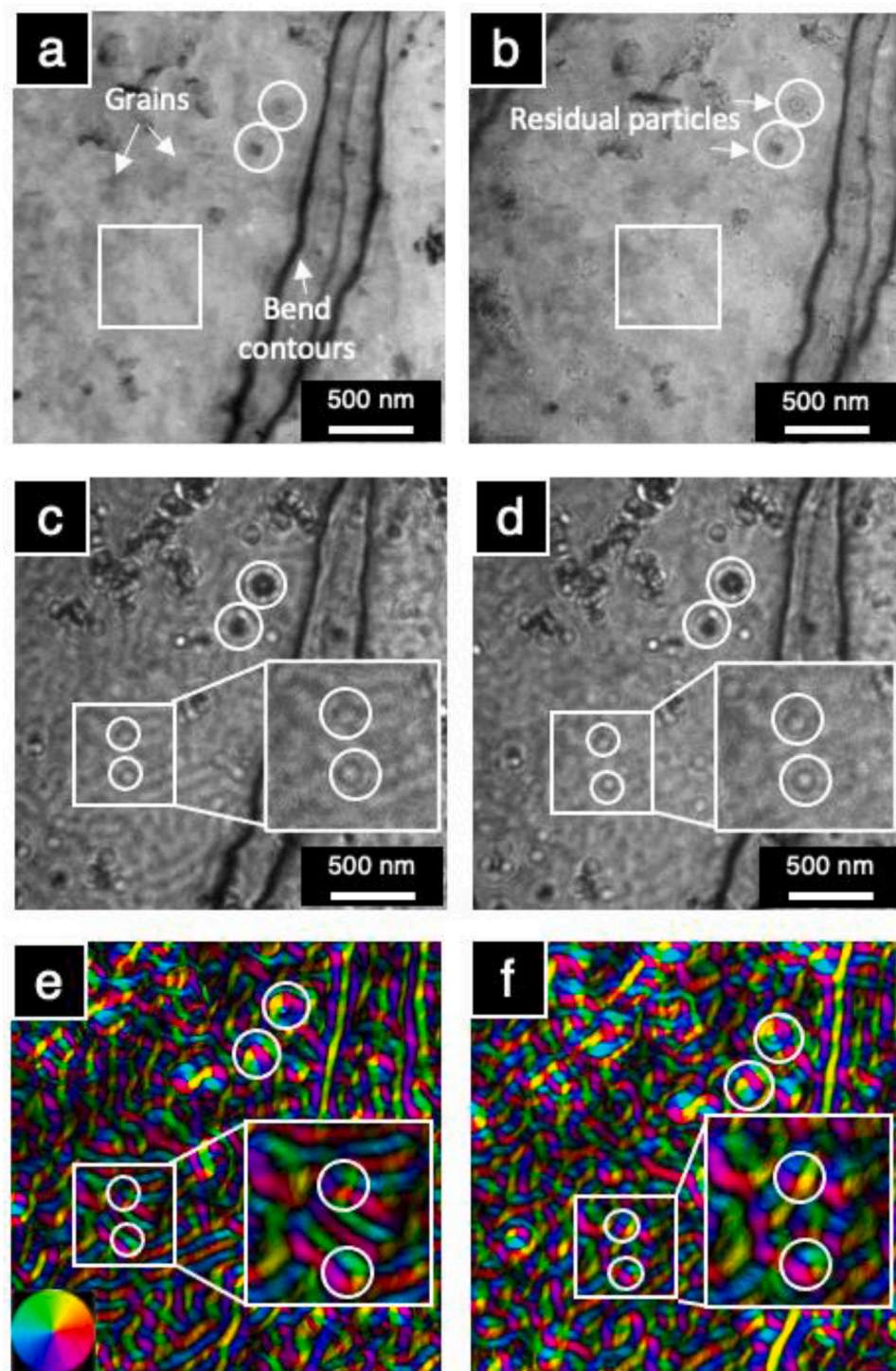


Fig. 4. LTEM series images from the same area acquired at 240 K: (a) 0 mT and (b) 80 mT in-focus; (c) 0 mT and (d) 80 mT 400 μm over-focused. Corresponding under-focus images not shown here. (e) 0 mT and (f) 80 mT IMI reconstruction maps obtained from defocused LTEM images with high pass filter of 5. The color wheel indicates the field direction. The white circle in the images highlighted same residual particles as reference markers. Regions in white box are magnified to show the transition from the helical phase at 0 mT to skyrmions at 80 mT.

on the sample; when the diffraction and optical conditions are close between the original image and the subtracted image, these features are not clearly observed, but when the differences are maximized, it becomes clearer.

3.2. Frequency filtered CoM-DPC reconstructed from Lorentz 4D-STEM dataset

Fig. 7 shows the reconstructed virtual BF images and IMI maps obtained from the same region with different convergence semi-angles and collection semi-angle ranges. The Lorentz 4D-STEM dataset were

acquired at 0 mT and 240 K. As explained in Section 3.1, the non-magnetic features can be readily seen in virtual BF images (Fig. 7a,d). To minimize the contrast contribution from these features (background contrast), it needs a combination of convergence angle and collection angle range that covers the spatial frequencies of magnetic textures while the spatial frequencies of background contrast are mostly excluded, as discussed in Section 2.2.2.

In Fig. 7b and c, IMI maps are reconstructed using virtual masks from scattering angle range $(0-0.5)\alpha$ and $(0.75-1)\alpha$, respectively. Here, we have a pre-knowledge that the spatial width of the magnetic helical phase in FeGe is $\sim 223\text{C}$ 50–70 nm [39]. In Fig. 7b, the transmitted core

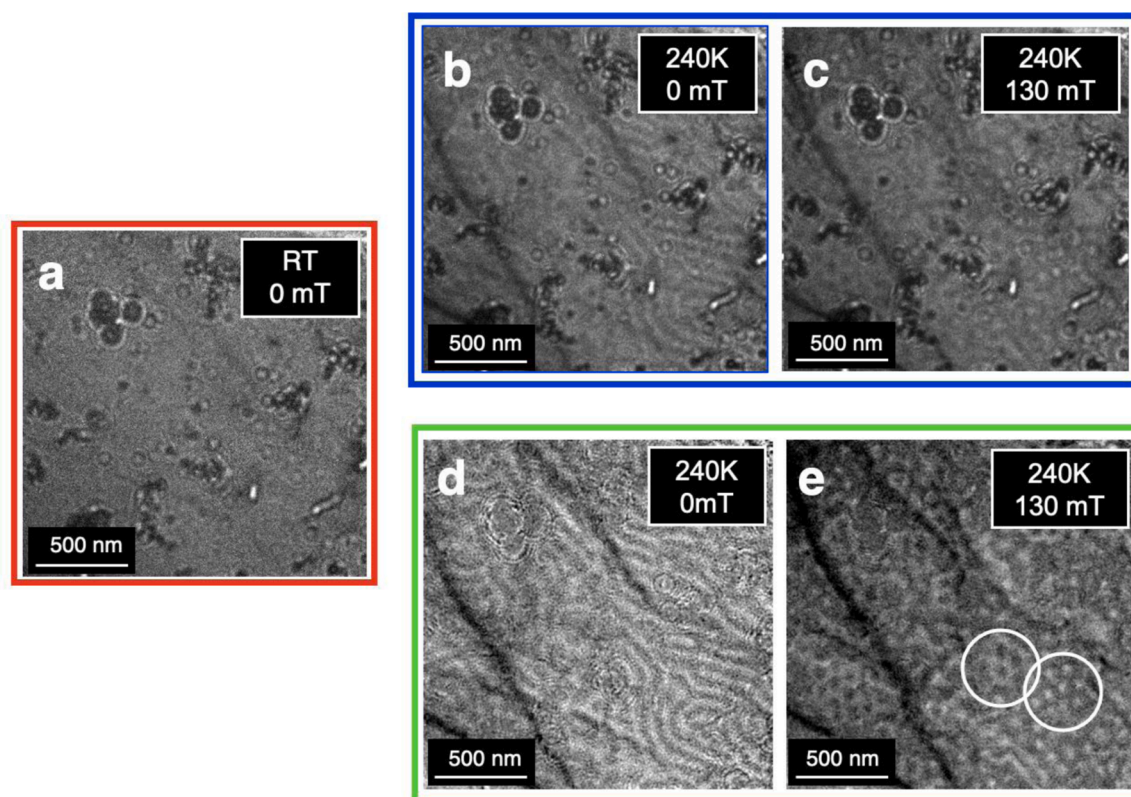


Fig. 5. Enhanced magnetic contrast in LTEM images. (a) Defocused LTEM image acquired at RT and 0 mT used as a background contrast image. (b) Defocused LTEM image acquired at 240 K and 0 mT. (c) Defocused LTEM image acquired at 240 K and 130 mT. (d) Background removed LTEM image from (b). (e) Background removed LTEM image from (c). The temperature and magnetic field are labeled at top right corner in each image. White circles in (e) indicate regions where skyrmions have opposite chirality. The defocus was fixed to be 200 μm .

spatial frequency range (3.4 nm, 20.2 nm) is in a higher range than spatial frequencies of magnetic contrast. Therefore, the contrast in Fig. 7b mainly comes from short-ranged components in background, such as grains, bend contours and residual particles. In contrast, selecting transmitted disk edge, $(0.75-1)\alpha$, means that CTF includes both short-range and long-rang spatial frequencies above $\sim x223C$ 2.5 nm. Consequently, one can observe the coexistence of magnetic contrast of helical phase and background contrast in Fig. 7c. These results are consistent with the recently reported work on FeGe thin film [15]. Better resolved magnetic contrast can be established by selecting a smaller convergence angle of $\sim x223C$ 60 μrad . As shown in Fig. 7e, helical phase is clearly distinguishable when we selected a spatial frequency range of (21.9 nm, 131.2 nm). Including a larger collection angle range does not enhance further the magnetic contrast but introduces diffraction contrast from particle defects and grains, see Fig. 7f.

Having established a method to enhance magnetic phase contrast in Lorentz 4D-STEM, we explored if the helical-skyrmion phase transition can be observed. The results are shown in Fig. 8. The reconstructed virtual BF images are shown in Fig. 8a,c, where residual particles linked with white dashed lines are used as reference markers. After applying 80 mT magnetic field, the helical phase in Fig. 8b is transformed into a skyrmion phase in Fig. 8d. In addition, skyrmion chirality can be distinguished directly from the IMI maps. However, the spatial frequency filtering method cannot distinguish magnetic texture from the mixed contrast of magnetic texture, defects, and bend contours if they span similar spatial frequency ranges. This can be observed from the defect rich regions in Fig. 8 where one can observe contrast change when applied field while the magnetic texture cannot be resolved from the unwanted contribution from defects and bend contour.

3.3. Registration of 4D-STEM datasets acquired at different tilt angles

Most features contributing to background contrast in LSTEM are sensitive to sample tilt. Therefore, registration of images acquired at different tilt angles can help to enhance the magnetic contrast by minimizing background contrast. Recent work has explored image registration to improve the phase contrast in a series of DPC images acquired using segmented detectors [17]. Here, we extended this method to 4DSTEM datasets acquired at different sample tilt angles. Fig. 9a-c show reconstructed BF images and IMI maps from three 4DSTEM datasets acquired with varied sample tilts ($< 1^\circ$ along horizontal or vertical axis). In each image, one can observe the redistribution of bend contours and grain contrast since they are sample tilt sensitive. Following the image steps in Section 2.2.3, we registered three 4DSTEM dataset into a new one. Comparing the reconstructed BF and IMI maps, we can find the contrast from bend contours decreased after the registration average, as shown in the highlighted red dashed boxes in Fig. 9d. Therefore, this method can help to get a more reliable phase contrast interpretation. However, Fig. 9d still contains some contrast that cannot be considered as magnetic origin, such as the strong contrast near the specimen boundaries and defects. As we mentioned in Section 2.2.3, if their distribution does not change randomly when tilting the sample, these residual diffraction contrasts cannot be suppressed. In addition, when the objective lens in the microscope is activated, specimen tilting will create in-plane fields in the sample. The presence of in-plane fields may affect the behavior of the magnetic texture in the in-plane field sensitive magnet.

4. Discussion

By using the phase contrast enhancement methods presented here,

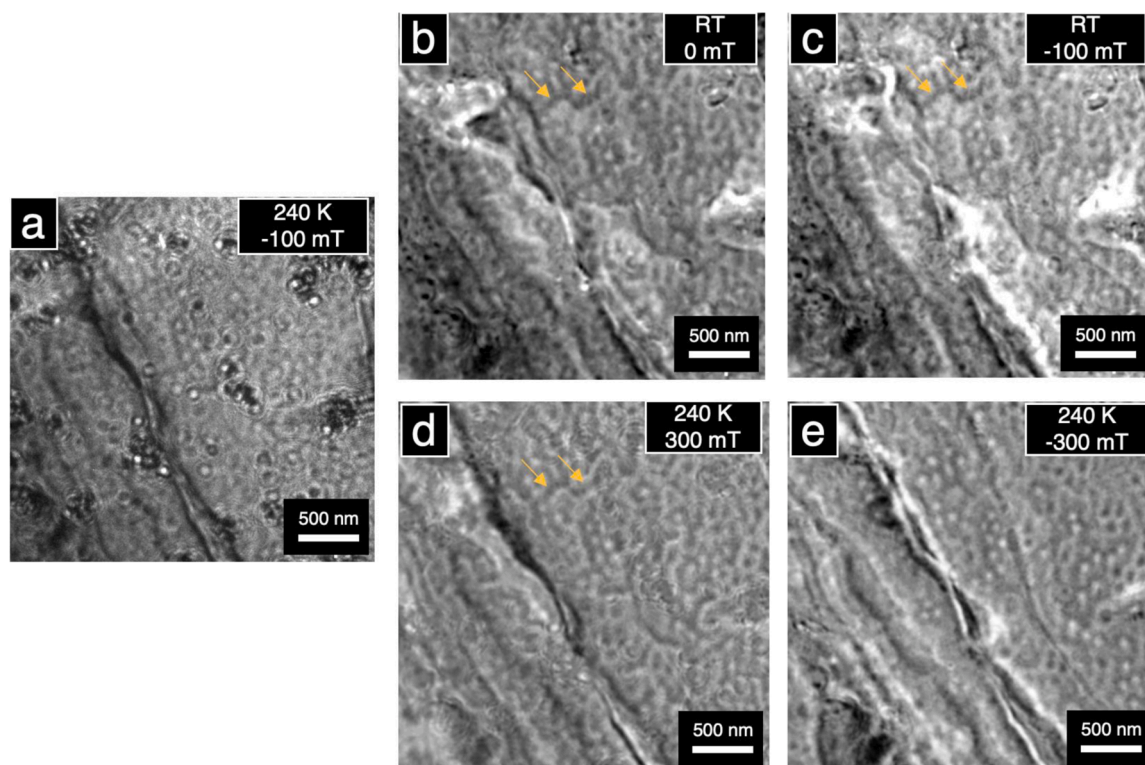


Fig. 6. Enhanced magnetic contrast in LTEM images after background subtraction using background images obtained at different conditions. (a) Original defocused LTEM image acquired at 240 K and -100 mT. (b)-(e) resulting images after subtraction of background images acquired at (b) RT and 0 mT (c) RT and -100 mT, (d) 240 K and 300 mT, and (e) 240 K and -300 mT. Yellow arrows point additional contrast observed in (b), (c) and (d). The defocus was fixed to be 200 μm (For interpretation of the references to color in this figure legend, the reader is referred to the web version of this article.).

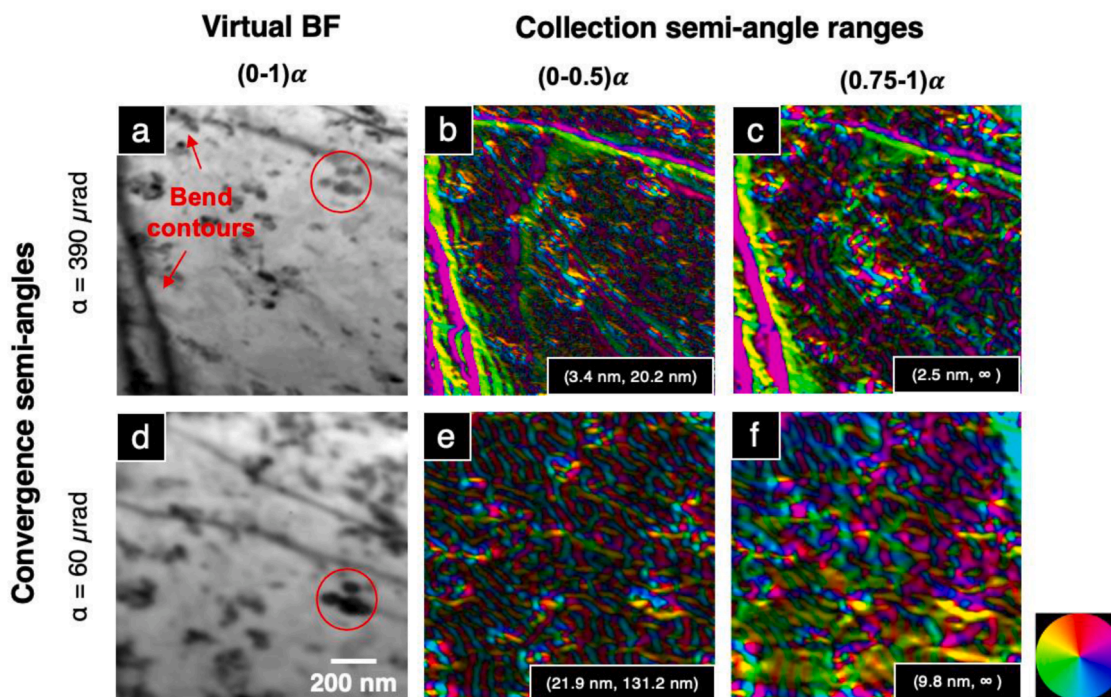


Fig. 7. Images obtained from Lorentz 4D-STEM datasets that acquired from plan-view FeGe thin films at 240 K. (a), (d) Virtual BF images reconstructed from $(0 - 1)\alpha$. (b), (e) IMI map reconstructed from $(0 - 0.5)\alpha$. (c), (f) IMI map reconstructed from $(0.75 - 1)\alpha$. The convergence semi-angle is $\sim 223^\circ$ 390 μrad in (a)-(c) and $\sim 223^\circ$ 60 μrad in (d)-(f). The transmitted spatial frequency ranges in reconstructed IMI maps are labeled at the bottom right (more details see Section 2.2.2). Color wheel indicates the field direction. Same particle defects are highlighted in virtual BF maps with red circles. The blurring in (d) is due to the high spatial frequencies are limited with small convergence semi-angles.

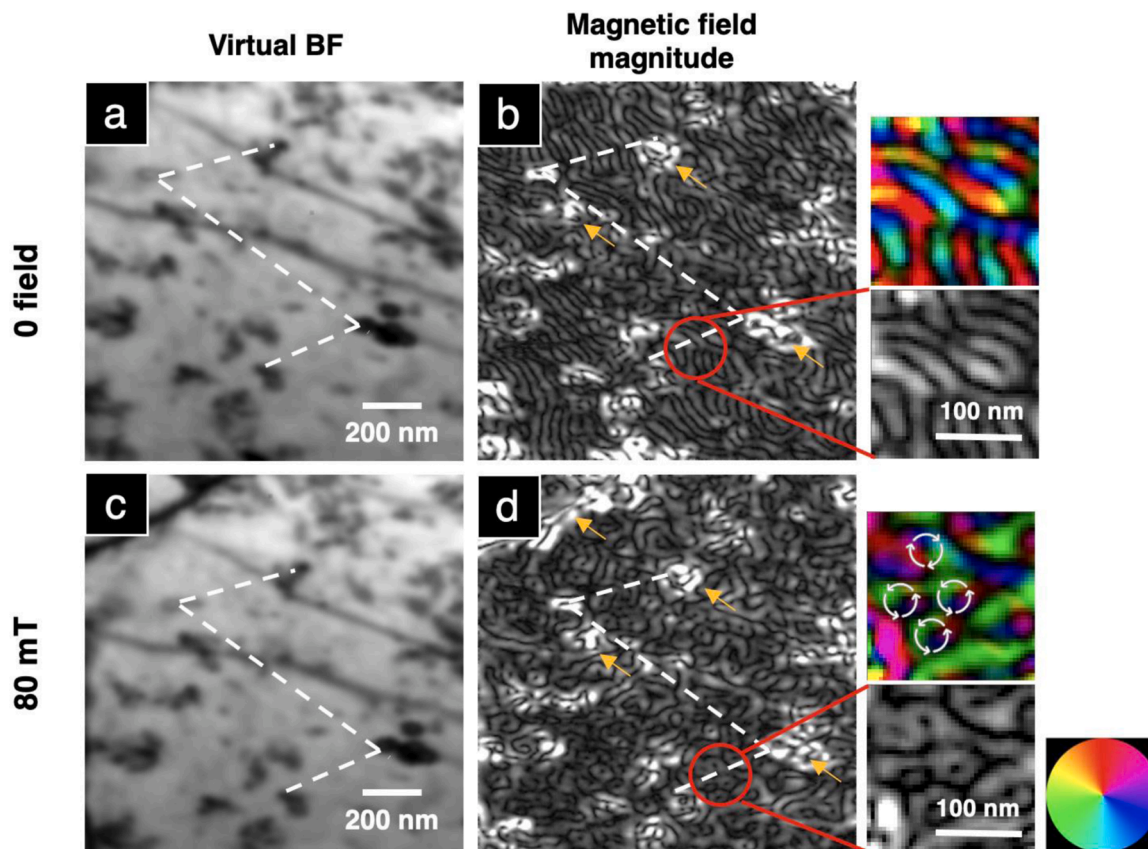


Fig. 8. Virtual BF image and CoM DPC IMI map obtained from 4D-STEM dataset of planar view FeGe thin films at 240 K with convergence angle $\sim 223 \times 60 \mu\text{rad}$. (a) The virtual BF image reconstructed from scattering angle range (0 – 1) at 0 mT. (b) The CoM IMI map reconstructed from scattering angle range (0 – 0.5) at 0 mT. (c) The virtual BF image reconstructed from scattering angle range (0 – 1) at 80 mT. (d) The CoM IMI map reconstructed from scattering angle range (0 – 0.5) at 80 mT. White dashed lines connected defects for reference to see magnetic phase transformation regions between helical and skyrmions. The region in the red circle is magnified together with a color figure showing spin direction while the orange arrows point out regions with mixed contrast of magnetic textures, defects, and bend contour. The scale bar in the magnified maps is 100 nm while the color wheel indicates the field direction.

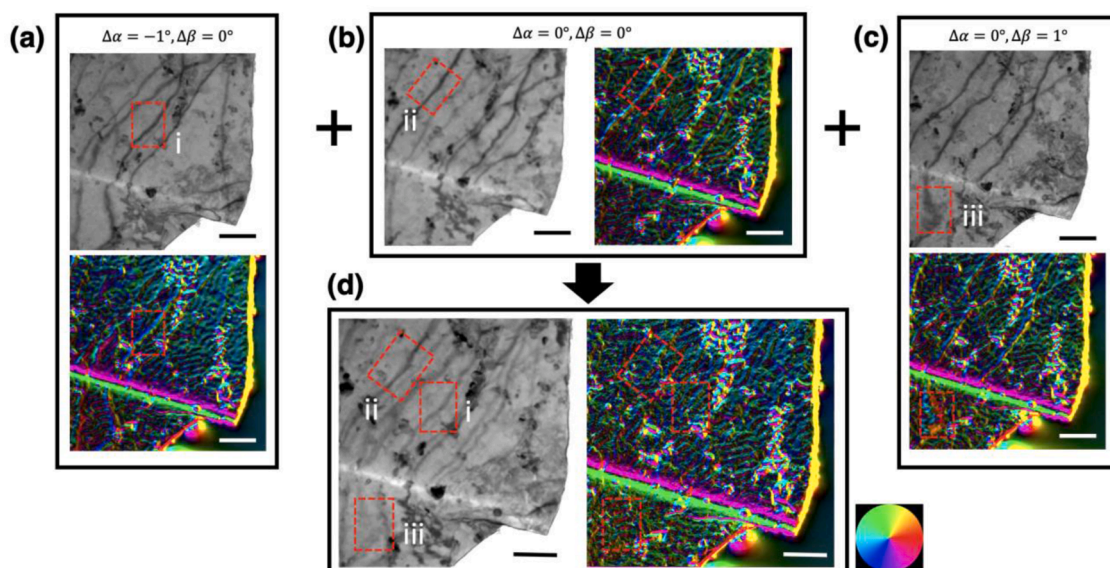


Fig. 9. Virtual BF image and CoM IMI map obtained from 4D-STEM dataset of planar view FeGe thin films at 253 K and 0 mT with different sample tilting angles. Note that the datasets are acquired at 0 mT to avoid any potential contribution from in-plane fields. (a-c) are reconstructed images from raw 4D-STEM datasets at different sample tilting angles of $\Delta\alpha$ and $\Delta\beta$. (d) are reconstructed images from averaged 4D-STEM dataset of (a)-(c) after registration. The BF images are in gray and the IMI maps are in color, where the color wheel indicates the field direction. Dashed rectangular highlighted regions are some example of bend contours. The scale bar is 500 nm. The bright field and IMI maps are reconstructed from (0 – 1) and (0.75–1), respectively.

we successfully imaged skyrmion and helical phase in a polycrystalline FeGe thin film sample in plan-view in both LTEM and LSTEM modes. In this section, we will summarize the advantages and challenges of three methods explored in this work.

LTEM in Fresnel mode provides a faster acquisition and larger field of view for imaging magnetic contrast than LSTEM. In this mode, the Lorentz lens are defocused so that domain boundaries can be observed as bright/dark lines. However, an abrupt change of projection potential can also result in such Fresnel fringes. Therefore, for non-ideal thin film samples with weak magnetic contrast, large defocus and post-processing are needed to extract magnetic contrast from complex background contrast. However, using larger defocus will change the optical conditions in microscope, and thus decrease the spatial resolution and change the image magnification. In addition, varying the objective lenses current to apply different fields will introduce a beam shift and image rotation, also affecting the defocus and beam intensity distribution. These make the reliable alignment of LTEM image series challenging in practice, especially if a large defocus is applied on a sample with weak magnetic phase contrast and complex backgrounds. Even LTEM background subtraction provides effective phase contrast enhancement after good alignment, it remains challenging to find the proper background image as shown in Section 3.1. In our case, even though we can get a good imaging of skyrmion phase with helicity inversion, IMI map from background subtracted images is not implemented because it requires alignment of a series of images at different defocus, and contains negative components.

The reconstruction of CoM-DPC from Lorentz 4D-STEM datasets can provide better spatial resolution in IMI maps. By understanding the phase contrast transmission function of CoM-DPC, it is possible to filter out specific spatial frequencies by a combination of the beam convergence angle and collection angle ranges. In this work, we demonstrated that the frequency filtered Lorentz 4D-STEM method provides a method comparable to the LTEM background subtraction, and in addition to provides an IMI map. Although spatial frequency selection may limit the spatial resolution of magnetic features, it is a trade-off for a better signal-to-noise ratio, i.e. the high-frequency signal (higher resolution) information is filtered out since it includes more background signal. However, this approach also has some challenges, requiring not only a prior understanding of the spatial frequency of the magnetic phase in the sample, but also an optimal convergence angle, which is limited by the range of convergence angles available in the microscope. In addition, the phase-contrast reconstruction using this technique is sensitive to any background in which transmission disk strength redistribution is introduced. Reliable interpretation of pure magnetic phases can be challenging if the background contrast is similar to the spatial frequency of the magnetic phase, or if they are too strong to break the weak phase approximation.

The registration of Lorentz 4DSTEM at different sample tilt angles provides an alternative method to minimize sample tilt sensitive background contrast. However, there are three main challenges that can limit its application. Firstly, if there is an external magnetic field, it will introduce in-plane field. The presence of in-plane fields should not affect electric field imaging but is critical for many in-plane field sensitive magnets. Secondly, for non-randomly distributed magnetic contrast, it is necessary to explore a large sample tilting series, which is a challenge from both an experimental and data processing perspective. Finally, a sample tilt causes changes to the phase shifts since the integration trajectory changes, and therefore the combination of IMI maps for different sample tilts will decrease the spatial resolution of magnetic features. The combination of 4DSTEM and dynamic probe tilt system may be a more promising approach than sample tilt-series averaging method.

5. Conclusions

In summary, we used Lorentz TEM and Lorentz STEM to study the magnetic texture in a polycrystalline FeGe thin film (35 nm) grown on Si

substrate. The complex "background" contrast associated with defects and sample preparation artifacts make it difficult to directly image magnetic textures in this plan view sample. To separate magnetic contrast from the background comparison, we explored three post-processing methods: 1) background subtraction in defocused Lorentz-TEM images; 2) frequency filtered CoM-DPC reconstructed from Lorentz 4D-STEM dataset; 3) registration of 4D-STEM datasets acquired at different tilting angles. Using these methods, we have successfully achieved real spatial imaging of both helical and skyrmion phases in this plan-view specimen. The implementation of each method and its advantages/limitations is discussed in detail, providing insights that can be transferred to other non-ideal magnetic or electrical samples.

Funding

This work was primarily supported by DARPA under Grant No. D18AP00008. DWM acknowledges support from the Center for Emergent Materials at the Ohio State University, a National Science Foundation Materials Research Science and Engineering Center (Grant No. DMR- 2,011,876). BW acknowledges support from the Presidential Fellowship of the Ohio State University. Electron microscopy experiments were supported by the Center for Electron Microscopy and Analysis at the Ohio State University.

Data and materials availability

All data is available in the main text or the supplementary materials.

CRediT authorship contribution statement

Binbin Wang: Conceptualization, Formal analysis, Data curation, Software, Writing – original draft. **Núria Bagués:** Formal analysis, Data curation, Writing – review & editing. **Tao Liu:** Resources. **Roland K. Kawakami:** Resources. **David W. McComb:** Supervision, Writing – review & editing.

Declaration of Competing Interest

The authors declare that they have no known competing financial interests or personal relationships that could have appeared to influence the work reported in this paper.

Acknowledgments

We thank Dr. Bryan D. Esser, Dr. Austin Wade and Dr. Robert Williams for their assistance with the TEM and helpful discussions. We also thank Dr Stephen Boona for his assistance with the TKD measurements and Prof. David Muller for help discussion

References

- [1] N. Nagaosa, Y. Tokura, Topological properties and dynamics of magnetic skyrmions, *Nat. Nanotechnol.* 8 (2013) 899–911, <https://doi.org/10.1038/nnano.2013.243>.
- [2] X. Zhang, Y. Zhou, K.M. Song, T.E. Park, J. Xia, M. Ezawa, X. Liu, W. Zhao, G. Zhao, S. Woo, Skyrmion-electronics: writing, deleting, reading and processing magnetic skyrmions toward spintronic applications, *J. Phys. Condens. Matter.* (2020) 32, <https://doi.org/10.1088/1361-648X/ab5488>.
- [3] H.W. Fuller, M.E. Hale, Determination of magnetization distribution in thin films using electron microscopy, *J. Appl. Phys.* 31 (1960) 238–248, <https://doi.org/10.1063/1.1735552>.
- [4] J.N. Chapman, The investigation of magnetic domain structures in thin foils by electron microscopy, *J. Phys. D Appl. Phys.* 17 (1984) 623–647, <https://doi.org/10.1088/0022-3727/17/4/003>.
- [5] S. Bajt, A. Barty, K.A. Nugent, M. McCartney, M. Wall, D. Paganin, Quantitative phase-sensitive imaging in a transmission electron microscope, *Ultramicroscopy* 83 (2000) 67–73, [https://doi.org/10.1016/S0304-3991\(99\)00174-6](https://doi.org/10.1016/S0304-3991(99)00174-6).
- [6] K. Ishizuka, B. Allman, Phase measurement of atomic resolution image using transport of intensity equation, *J. Electron Microsc.* 54 (2005) 191–197, <https://doi.org/10.1093/jmicro/dfi024> (Tokyo).

- [7] J.M. Cowley, Twenty forms of electron holography, *Ultramicroscopy* 41 (1992) 335–348, [https://doi.org/10.1016/0304-3991\(92\)90213-4](https://doi.org/10.1016/0304-3991(92)90213-4).
- [8] C. Ophus, Four-dimensional scanning transmission electron microscopy (4d-stem): from scanning nanodiffraction to ptychography and beyond, *Microsc. Microanal.* (2019) 563–582, <https://doi.org/10.1017/S1431927619000497>.
- [9] N. Shibata, S.D. Findlay, Y. Kohno, H. Sawada, Y. Kondo, Y. Ikuhara, Differential phase-contrast microscopy at atomic resolution, *Nat. Phys.* 8 (2012) 611–615, <https://doi.org/10.1038/nphys2337>.
- [10] J. Tang, L. Kong, W. Wang, H. Du, M. Tian, Lorentz transmission electron microscopy for magnetic skyrmions imaging, *Chinese Phys. B* 28 (2019), 087503, <https://doi.org/10.1088/1674-1056/28/8/087503>.
- [11] L.C. Peng, Y. Zhang, S.L. Zuo, M. He, J.W. Cai, S.G. Wang, H.X. Wei, J.Q. Li, T. Y. Zhao, B.G. Shen, Lorentz transmission electron microscopy studies on topological magnetic domains, *Chinese Phys. B* 27 (2018), 066802, <https://doi.org/10.1088/1674-1056/27/6/066802>.
- [12] N. Bagues, B. Wang, T. Liu, C. Selcu, S. Boona, R. Kawakami, M. Randeria, D. McComb, Imaging of magnetic textures in polycrystalline FeGe thin films via *in-situ* Lorentz transmission electron microscopy, *Microsc. Microanal.* 26 (2020) 2020, <https://doi.org/10.1017/S1431927620019029>.
- [13] M. Hirschberger, T. Nakajima, S. Gao, L. Peng, A. Kikkawa, T. Kurumaji, M. Kriener, Y. Yamasaki, H. Sagayama, H. Nakao, K. Ohishi, K. Kakurai, Y. Taguchi, X. Yu, T. hisa Arima, Y. Tokura, Skyrmion phase and competing magnetic orders on a breathing kagomé lattice, *Nat. Commun.* 10 (2019) 1–9, <https://doi.org/10.1038/s41467-019-13675-4>.
- [14] M. Krajnak, D. McGrouther, D. Maneuski, V. O'Shea, S. McVitie, Pixelated detectors and improved efficiency for magnetic imaging in STEM differential phase contrast, *Ultramicroscopy* 165 (2016) 42–50, <https://doi.org/10.1016/j.ultramic.2016.03.006>.
- [15] Nguyen, K.X., Turgut, E., Cao, M.C., Glaser, J., Chen, Z., Stolt, M.J., Jin, S., Fuchs, G.D., Muller, D.A., Disentangling magnetic and grain contrast in polycrystalline FeGe thin films using 4-D Lorentz scanning transmission electron microscopy, arXiv preprint arXiv:2001.06900, 2020.
- [16] M.C. Cao, Y. Han, Z. Chen, Y. Jiang, K.X. Nguyen, E. Turgut, G.D. Fuchs, D. A. Muller, Theory and practice of electron diffraction from single atoms and extended objects using an EMPAD, *Microscopy*. 67 (2018) i150–i161, <https://doi.org/10.1093/jmicro/dfx123>.
- [17] Y.O. Murakami, T. Seki, A. Kinoshita, T. Shoji, Y. Ikuhara, N. Shibata, Magnetic-structure imaging in polycrystalline materials by specimen-tilt series averaged DPC STEM, *Microscopy* 69 (2020) 312–320, <https://doi.org/10.1093/jmicro/dfaa029>.
- [18] X.Z. Yu, N. Kanazawa, Y. Onose, K. Kimoto, W.Z. Zhang, S. Ishiwata, Y. Matsui, Y. Tokura, Near room-temperature formation of a skyrmion crystal in thin-films of the helimagnet FeGe, *Nat. Mater.* 10 (2011) 106–109, <https://doi.org/10.1038/nmat2916>.
- [19] A.S. Ahmed, J. Rowland, B.D. Esser, S.R. Dunsiger, D.W. McComb, M. Randeria, R. K. Kawakami, Chiral bobsbers and skyrmions in epitaxial FeGe/Si(111) films, *Phys. Rev. Mater.* 2 (2018), 041401, <https://doi.org/10.1103/PhysRevMaterials.2.041401>.
- [20] S.X. Huang, C.L. Chien, Extended skyrmion phase in epitaxial FeGe(111) thin films, *Phys. Rev. Lett.* 108 (2012), 267201, <https://doi.org/10.1103/PhysRevLett.108.267201>.
- [21] D.N. Mastronarde, S.R. Held, Automated tilt series alignment and tomographic reconstruction in IMOD, *J. Struct. Biol.* 197 (2017) 102–113, <https://doi.org/10.1016/j.jsb.2016.07.011>.
- [22] K. Ishizuka, B. Allman, Phase measurement of atomic resolution image using transport of intensity equation, *J. Electron Microsc.* 54 (2005) 191–197, <https://doi.org/10.1093/JMICRO/DFI024> (Tokyo).
- [23] B. Wang, B.D. Esser, N. Bagués, R.E.A. Williams, J. Yan, D.W. McComb, Quantifying Jahn-Teller distortion at the nanoscale with picometer accuracy using position averaged convergent beam electron diffraction, *Phys. Rev. Res.* 1 (2019), 032037, <https://doi.org/10.1103/physrevresearch.1.032037>.
- [24] J.M. Zuo, M. Kim, M. O'Keeffe, J.C.H. Spence, Direct observation of d-orbital holes and Cu-Cu bonding in Cu₂O, *Nature* 401 (1999) 49–52, <https://doi.org/10.1038/43403>.
- [25] N. Shibata, T. Seki, G. Sánchez-Santolino, S.D. Findlay, Y. Kohno, T. Matsumoto, R. Ishikawa, Y. Ikuhara, Electric field imaging of single atoms, *Nat. Commun.* 8 (2017) 2–4, <https://doi.org/10.1038/ncomms15631>.
- [26] B. Wang, N. Bagues, T. Liu, J. Yan, R. Kawakami, D. McComb, Spatial frequency selection in Lorentz 4D-scanning transmission electron microscopy reconstruction, *Microsc. Microanal.* (2020) 26, <https://doi.org/10.1017/S1431927620019777>.
- [27] Z. Chen, E. Turgut, Y. Jiang, K.X. Nguyen, G.C. Correa, M.J. Stolt, S. Jin, D. C. Ralph, G.D. Fuchs, D.A. Muller, Resolving internal magnetic structures of Skyrmions by Lorentz electron ptychography, *Microsc. Microanal.* 25 (2019) 32–33, <https://doi.org/10.1017/s1431927619000898>.
- [28] B.A. Lippmann, Ehrenfest's theorem and scattering theory, *Phys. Rev. Lett.* 15 (1965) 11–14, <https://doi.org/10.1103/PhysRevLett.15.11>.
- [29] K. Müller-Caspary, F.F. Krause, T. Grieb, S. Löffler, M. Schowalter, A. Béché, V. Galioit, D. Marquardt, J. Zweck, P. Schattschneider, J. Verbeeck, A. Rosenauer, Measurement of atomic electric fields and charge densities from average momentum transfers using scanning transmission electron microscopy, *Ultramicroscopy* 178 (2017) 62–80, <https://doi.org/10.1016/j.ultramic.2016.05.004>.
- [30] H. Yang, T.J. Pennycook, P.D. Nellist, Efficient phase contrast imaging in STEM using a pixelated detector. Part II: optimisation of imaging conditions, *Ultramicroscopy* 151 (2015) 232–239, <https://doi.org/10.1016/j.ultramic.2014.10.013>.
- [31] H.G. Brown, R. Ishikawa, G. Sanchez-Santolino, N. Shibata, Y. Ikuhara, L.J. Allen, S.D. Findlay, Large angle illumination enabling accurate structure reconstruction from thick samples in scanning transmission electron microscopy, *Ultramicroscopy* 197 (2019) 112–121, <https://doi.org/10.1016/j.ultramic.2018.12.010>.
- [32] I. Lazić, E.G.T. Bosch, S. Lazar, Phase contrast STEM for thin samples: integrated differential phase contrast, *Ultramicroscopy* 160 (2016) 265–280, <https://doi.org/10.1016/j.ultramic.2015.10.011>.
- [33] D.B. Williams, C.B. Carter, *The transmission electron microscope. The Transmission Electron Microscope*, Springer, 2009, pp. 3–22, https://doi.org/10.1007/978-0-387-76501-3_1.
- [34] B.H. Savitzky, L. Hughes, K.C. Bustillo, H.D. Deng, N.L. Jin, E.G. Lomeli, W. C. Chueh, P. Herring, A. Minor, C. Ophus, py4DSTEM: open source software for 4D-STEM data analysis, *Microsc. Microanal.* 25 (2019) 124–125, <https://doi.org/10.1017/s1431927619001351>.
- [35] M. Nord, R.W.H. Webster, K.A. Paton, S. McVitie, D. McGrouther, I. Maclaren, G. W. Paterson, Fast pixelated detectors in scanning transmission electron microscopy. part i: data acquisition, live processing, and storage, *Microsc. Microanal.* 26 (2020) 653–666, <https://doi.org/10.1017/S1431927620001713>.
- [36] C.M. O'Leary, B. Haas, C.T. Koch, P.D. Nellist, L. Jones, Increasing spatial fidelity and SNR of 4D-STEM using multi-frame data fusion, *Microsc. Microanal.* (2021), <https://doi.org/10.1017/S1431927621012587>.
- [37] B. Haas, M. Schloz, A. Mittelberger, T. Lovejoy, J. Müller, O. Krivanek, L. Jones, W. Van Den Broek, C. Koch, Comparison of ptychography vs. center-of-mass analysis of registered 4D-STEM series, *Microsc. Microanal.* 26 (2020) 1898–1900, <https://doi.org/10.1017/S1431927620019765>.
- [38] L. Jones, H. Yang, T.J. Pennycook, M.S.J. Marshall, S. Van Aert, N.D. Browning, M. R. Castell, P.D. Nellist, Smart Align-a new tool for robust non-rigid registration of scanning microscope data, *Adv. Struct. Chem. Imaging* 1 (2015) 1–16, <https://doi.org/10.1186/s40679-015-0008-4>.
- [39] X.Z. Yu, N. Kanazawa, Y. Onose, K. Kimoto, W.Z. Zhang, S. Ishiwata, Y. Matsui, Y. Tokura, Near room-temperature formation of a skyrmion crystal in thin-films of the helimagnet FeGe, *Nat. Mater.* 10 (2011) 106–109, <https://doi.org/10.1038/nmat2916>.